Effects of Chlorine Mixing on Optoelectronics, Ion-Migration and Gamma-ray Detection In Bromide Perovskites

Nikita Rybin, Dibyajyoti Ghosh, Jeremy Tisdale, Shreetu Shrestha, Michael Yoho, Duc Duy Vo, Jacky Even, Claudine Katan, Wanyi Nie, Amanda J Neukirch, et al.

▶ **To cite this version:**

Nikita Rybin, Dibyajyoti Ghosh, Jeremy Tisdale, Shreetu Shrestha, Michael Yoho, et al.. Effects of Chlorine Mixing on Optoelectronics, Ion-Migration and Gamma-ray Detection In Bromide Perovskites. Chemistry of Materials, 2020, 32 (5), pp.1854-1863. 10.1021/acs.chemmater.9b04244 . hal-02478539

HAL Id: hal-02478539
https://hal.science/hal-02478539v1

Submitted on 17 Mar 2020

HAL is a multi-disciplinary open access archive for the deposit and dissemination of scientific research documents, whether they are published or not. The documents may come from teaching and research institutions in France or abroad, or from public or private research centers.

L'archive ouverte pluridisciplinaire **HAL**, est destinée au dépôt et à la diffusion de documents scientifiques de niveau recherche, publiés ou non, émanant des établissements d'enseignement et de recherche français ou étrangers, des laboratoires publics ou privés.

Effects of Chlorine Mixing on Optoelectronics, Ion-Migration and Gamma-ray Detection In Bromide Perovskites

Nikita Rybin,[†,‡] Dibyajyoti Ghosh,[*,‡,¶] Jeremy Tisdale,[§] Shreetu Shresta,[§] Michael Yoho,[‖] Duc Vo,[‖] Jacky Even,[⊥] Claudine Katan,[#] Wanyi Nie,[§] Amanda Joy Neukirch,[‡] and Sergei Tretiak[*,‡,¶,@]

†*Skolkovo Institute of Science and Technology, Moscow 121205, Russia*

‡*Theoretical Division, Los Alamos National Laboratory, Los Alamos, NM, 87545, USA*

¶*Center for Nonlinear Studies, Los Alamos National Laboratory, Los Alamos, NM, 87545, USA*

§*Materials Physics and Applications Division, Los Alamos National Laboratory, Los Alamos, NM, 87545, USA.*

‖*Nuclear Engineering and Nonproliferation Division, Los Alamos National Laboratory, Los Alamos, NM, 87545, USA.*

⊥*Univ Rennes, INSA Rennes, CNRS, Institut FOTON - UMR 6082, F-35000 Rennes, France*

#*Univ Rennes, ENSCR, INSA Rennes, CNRS, ISCR - UMR 6226, F-35000 Rennes, France*

@*Center for Integrated Nanotechnologies, Los Alamos National Laboratory, Los Alamos, NM, 87545, USA*

E-mail: dibyajyoti@lanl.gov; serg@lanl.gov

Abstract

Controlled anion-mixing in halide perovskites has been shown to be an effective route to precisely tuning optoelectronic properties, in order to achieve efficient photovoltaic, light emission and radiation detection devices. However, an atomistic understanding behind the precise mechanism impacting the performances of mixed halide perovskite devices, particularly as a radiation detector, is still missing. Combining high-level computational methods and multiple experiments, here we systematically investigate the effect of chlorine (Cl) incorporation on the optical and electronic properties, structural stability, ion-migration as well as the γ-ray radiation detection ability of $MAPbBr_{3-x}Cl_x$. We observe that precise halide mixing suppresses bromide ion migration and consequently reduces the dark current by close to a factor of two, which significantly increases the resistance of the mixed-anion devices. Furthermore, reduced carrier effective masses and mostly unchanged exciton binding energies indicate enhanced charge carrier transport for these perovskite alloys. At the atomistic level, modifications to ion migration and charge carrier transport properties improve electronic properties and predominantly contribute to the better response and resolution in high-energy γ-ray detection with $MAPbBr_{3-x}Cl_x$, as compared to $MAPbBr_3$. This study provides a systematic approach to enhance the high-energy radiation detection ability of $MAPbBr_{3-x}Cl_x$-based devices by understanding the atomistic properties underpinning performance.

Introduction

Halide hybrid and inorganic perovskites have emerged as some of the most promising candidates for next-generation photovoltaic materials in the last decade.[1–7] In addition to solar cells, these materials demonstrate potential in various applications, ranging from light emitting diodes and photodetectors, to high-energy radiation sensors.[8–10] The realization of several beneficial properties like long and balanced diffusion lengths for electrons and holes, high absorption coefficients spanning the entire visible range, robust defect tolerance, and

highly tunable optical band gaps make halide perovskites very attractive materials for a wide range of applications.[11–13] Particularly, the presence of heavy elements in these dense materials, along with outstanding charge transport properties, indicate their potential use as detectors for high-energy radiations.[8,14–17] Preliminary studies have reported γ-ray detection with a reasonable resolution using bromide-based hybrid perovskites.[18]

Compositional engineering of halides has widely been adopted to improve the stability and enhance the performance of halide perovskite devices.[19–27] Several groups have explored halide mixing in detail for multivarious purposes such as color management, better crystallization and tuning the band gaps for tandem solar cells.[11,28–31] Due to the numerous beneficial effects, most of the highly efficient perovskite solar cells are of mixed halide compositions. In this regard, chlorine (Cl) incorporation was reported to dramatically improve diffusion lengths of carriers in $MAPbI_3$.[11,28–30] However, the presence of Cl in bulk $MAPbI_3$ and its exact impact on the optoelectronic properties has been highly debated in recent years.[31–34] Most of the reports have indicated that Cl can form a solid solution with Br and stay in the bulk of $MAPbBr_3$.[35–37] The relatively small difference in ionic radii and electronegativity between Br and Cl allows these anions to form solid solutions of mixed-anion halide perovskites. Due to the large band gap (> 2 eV), bromide based perovskites are not suitable for single-junction solar cells. However, they have been extensively used for LEDs and photodetector devices.[8,9,38,39] Cl incorporation in $MAPbBr_3$ precisely tunes the emission color for LEDs and response spectrum for photodetectors. Furthermore, $MAPbBr_{3-x}Cl_x$ thin films exhibit significantly prolonged recombination lifetime with finely tuned Cl concentrations. For high-energy radiation detection, $MAPbBr_3$ is one of the first hybrid perovskite materials to show promising results with significant response to charged particles.[40,41] Afterwards, hybrid and non-hybrid lead halide perovskites showed promising results for low-cost γ-ray detectors, including $MAPbI_3$,[42] and $CsPbBr_3$.[15] It was shown later that $MAPbBr_3$ responds not only to charged particles, but also to neutrons and γ-rays. However, the response to γ-ray was found to be weak for this material.[43] Nevertheless, recent experiments

have demonstrated the positive influence of Cl incorporation in $MAPbBr_3$, such as increased resistivity and reduced device noise of these materials. A small Cl concentration ($\approx 2\%$ molar ratio) has been found to dramatically enhance the resolution for γ-ray detection under a small electric field.[18] Despite all of these fascinating reports, a systematic and in-depth atomistic understanding on the effects of anion mixing for γ-ray detection of $MAPbBr_{3-x}Cl_x$ is largely absent.

In the present work, we combine experimental and computational efforts to thoroughly investigate the optoelectronic properties of $MAPbBr_{3-x}Cl_x$, particularly focusing on the small Cl concentration range ($x \leq 0.45$). We demonstrate that within this concentration regime, Cl is incorporated into the bulk of the material. Our atomistic level investigations find that anion-mixing partially suppresses the Br migration and enhances the charge carrier transport in these materials. These modifications significantly benefit the γ-ray detection response at room temperature. This study offers a guideline for improving radiation detection properties of hybrid bromide perovskites with an in-depth atomistic understanding of compositional tuning.

Results and Discussion

First, we evaluate numerically the thermodynamic stability of mixed anion $MAPbBr_{3-x}Cl_x$ lattices with respect to the corresponding monoanionic perovskites. As shown in Figure 1a, the calculated Helmholtz free energy (see Methods and section S1 in SI for details) of mixing for all the studied Cl concentrations is negative, indicating a stabilized solid solution of Br and Cl in these lattices. With increasing temperature, the solid solutions become more stable due to a significant entropic contribution to the free energy of mixing. Thus, our computational study indicates incorporation of Cl into the bulk of $MAPbBr_3$, forming mixed Br/Cl lattices. These results are in agreement with recent experimental and computational studies, where solid solution formation has been reported for Br/Cl mixing at room temperature.[44–49] Two

competing factors, strengths of ionic Pb-X bonds (X=Cl, Br) and strain energy due to the size mismatch between halides, dominantly affect the internal energies of $MAPbBr_{3-x}Cl_x$ crystals.[49,50] Compared to Br, Cl atoms form stronger ionic bonds with Pb^{2+} due to their higher electronegativity. As reported for similar perovskites, these stronger ionic bonds yield sufficient Coulomb energy to overcome the strain energy that arises from the size mismatch between the halide atoms.[49,50] Thus, at a lower concentration limit (up to 25 mol%), the solid solution of anions shows increased stability compared to the phase separated constituents of $MAPbBr_3$ and $MAPbCl_3$. The entropy of mixing, which arises due to anion mixing, stabilizes the mixed anion lattices further, exhibiting prominent thermodynamic stability of $MAPbBr_{3-x}Cl_x$ at room temperature. Similar entropy of mixing induced stability has also been reported for mixed A-cation perovskites.[21,51]

To provide evidence of controlled anion mixing in the experimental single crystals, we further explore the structural and optical changes in $MAPbBr_{3-x}Cl_x$ (Figure 1b-d). As shown in Figure 1b, the experimentally measured unit cell volumes (measured via powder X-ray diffraction on finely ground single crystals) reduce with increased Cl concentration, unambiguously showing successful anion mixing in these samples. The results shown in Figure S1 and Table S1 exhibit a quasi-linear trend in the experimentally determined cubic lattice parameter values with increased Cl concentration, decreasing from $a = 5.92$ Å to $a = 5.85$ Å, for $MAPbBr_3$ and $MAPbBr_{2.4}Cl_{0.6}$, respectively. The experimental lattice volume was then calculated based on the $Pm\bar{3}m$ cubic structure, as explained in the Experimental Procedure later. Similar lattice contraction in $MAPbBr_{3-x}Cl_x$ with increased Cl concentration has been reported previously as well.[8,45,52–55] It is worth to mentioning that, quasi-linear trend of lattice contraction for Br/Cl-mixed lattices is in agreement with the $MAPbI_{3-x}Br_x$ systems as reported earlier by Noh *et al.*[52]

Computationally optimized ground state structures of orthorhombic $MAPbBr_{3-x}Cl_x$ (see Methods) corroborate the trend of reduced lattice parameters and volume with Cl inclusion as shown in Figure 1b (black solid line). Although the extent of the reduction differs, the overall

trend in decreasing unit cell volume is in agreement between calculations and experimental observations. The difference in the extent of volume reduction can originate due to the fact that the experimental data corresponds to thermally expanded quasi-cubic structures, where the MA cation rotations are activated, while in the computational study, supercells are of the low-temperature orthorhombic phase with static A-cations. Detailed discussion is included in section S2 in SI. The smaller ionic radii for Cl with respect to Br, (r_{Cl} (1.67 Å) $< r_{Br}$ (1.84 Å)) and consequently shorter bond length of Pb-Cl than Pb-Br bonds, (see Fig. S2) is the apparent cause for this change in lattice volume. Thus, unlike the $MAPbI_{3-x}Cl_x$ systems,[11,28–30,32–34] our combined computational and experimental studies unambiguously demonstrate that at lower concentrations (up to 20 mol%), Cl prefers to be incorporated into the $MAPbBr_3$ lattice, via substitution of Br atoms, instead of inhomogeneous accumulation on the surfaces and interfaces.

We further characterize the optical properties of $MAPbBr_{3-x}Cl_x$ ($0 \leq x \leq 0.6$). To experimentally study changes in the band gap as a function of Cl incorporation, we examine the UV-Vis absorption (Figure 1c) and photoluminescence (Figure 1d) properties. Because of the 2 mm thick crystals, UV-Vis spectra were extracted from transmission measurements and converted to Tauc plots to estimate the optical band gaps. Other than the calculated band gaps, we also differences among the chlorine concentrated crystals in the above band gap regime of the absorption. For the 0%, 2%, and 5% Cl-incorporated crystals, the band edge is clear, and the above band gap regime is smooth. However, with the 10%, 15% and 20% Cl-incorporated crystals, we notice that the band edge is not as sharp with double features and the above band gap regime is noisy. We contribute this to the quality of the crystals grown, as we found when doping with >10% Cl, the crystal quality heavily decreases, showing cloudiness and microcracks, leading to the noisy signals in the absorption data.

There is a prominent linear trend, as the band gap of the single crystals increase as a function of Cl concentration (Figure S3a). The photoluminescence (Figure 1d) also shows the same trend, where we observe a gradual blue shift in the band gap of the single crystals

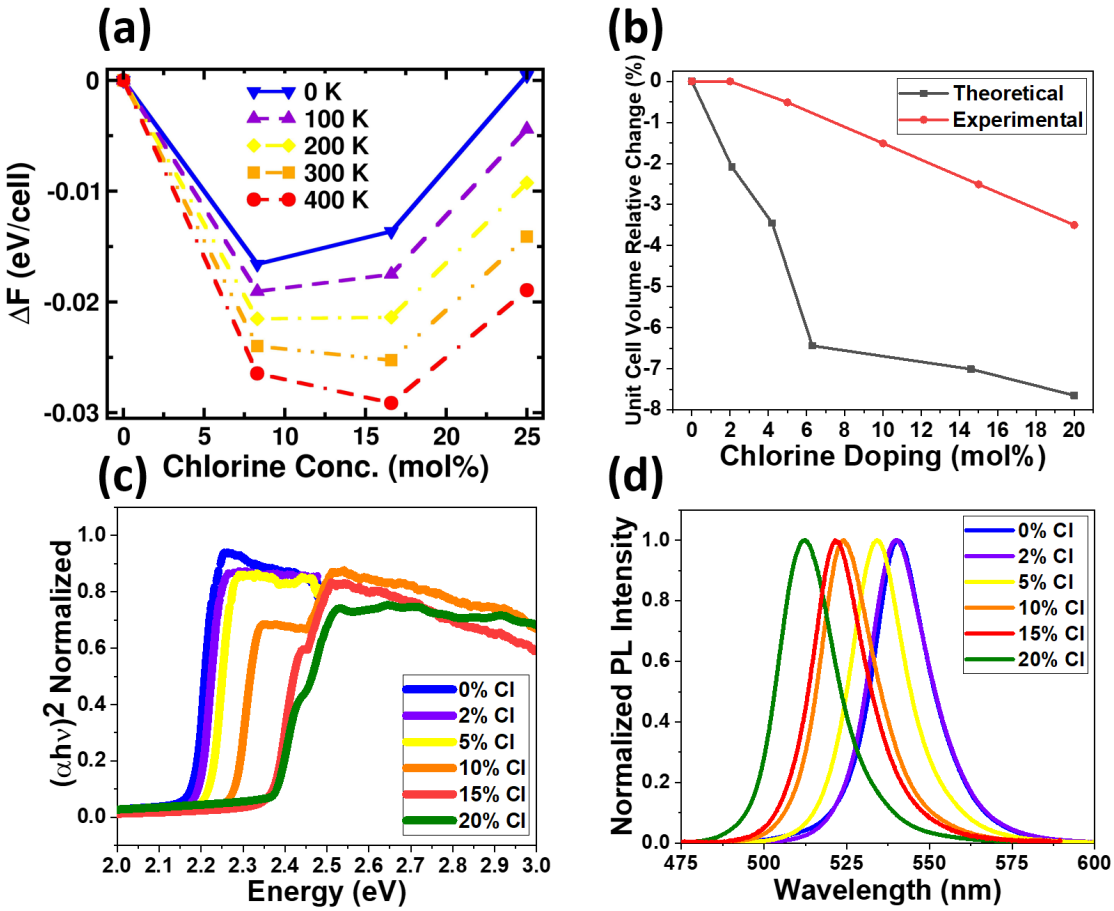

Figure 1: Effect of Cl incorporation in $MAPbBr_{3-x}Cl_x$. (a) Computational Helmholtz free energy as a function of Cl mol% and temperature, (b) Relative change in unit cell volume as a function of Cl concentration from computational calculations and experimental powder XRD, (c) Experimental UV-Vis absorption spectra and (d) emission spectra.

as the Cl concentration is increased (see Figure S3b). In parallel, we computationally evaluated the band gap variation in these mixed halide perovskites including spin-orbit coupling (SOC) effects for the heavy-element Pb and the hybrid (HSE06) functional (see Methods). As presented in Figure S4, the calculated band gaps blue-shift with the increased Cl concentration, in agreement with the experimental results. Note that, computationally evaluated band gap values are underestimated by ≈ 0.4 eV due to insufficient inclusion of the exact Hartree-Fock exchange term in the HSE06 functional. This systematic underestimation of the band gap using the HSE06 functional is well known and has been previously reported for other halide perovskites.[13,21,27,56] Moreover, the computed absorption spectra (Figure S5)

and corresponding calculated band gaps (Figure S3) calculated by the semi-local exchange-correlation functional, i.e. GGA-PBE functional, show better agreement with experimental data due to an incidental error cancellation of the SOC and electron-electron interaction terms.[57]

Next, we investigate the ion migration in these materials and its impact on current-voltage properties of the devices.[58–60] Ion transport induced phenomena underpin current-voltage hysteresis, switchable photovoltaics and polarization effects, and limit the application of hybrid perovskites in the field of solar cells and radiation detection.[61–64] Recently, compositional engineering with A-cations in iodide perovskites has been demonstrated as a promising approach to partially suppress the ion migration.[65] Here we investigate computationally and experimentally the effect of varying anion composition on the ion migration in $MAPbBr_{3-x}Cl_x$.

We computationally calculate activation energy barriers for the vacancy-assisted halide ion hopping in these mixed anion perovskites with the dispersion corrected DFT-based climbing image nudged elastic band (CI-NEB) approach (see Methods).[66] Note that we focus only on the halide diffusion, as previous studies report much higher activation barriers for Pb^{2+} and MA^{+} ions, due to the significant rearrangements in the local structure.[65,67,68] Since we have considered the low-symmetry orthorhombic phase of $MAPbBr_{3-x}Cl_x$, two inequivalent migration paths for Br/Cl have been modeled: (1) Br/Cl migration from equatorial to apical site and (2) Br migration from equatorial to equatorial site. In our calculations (see Methods), the initial and final configurations of the migration path were well converged in order to avoid severe underestimation of barrier energies. In $MAPbBr_3$, we find the activation energies of 0.24 eV and 0.33 eV, for Br migrating from equatorial to equatorial and equatorial to apical site, respectively (see Figure 2a and Figure S6, S7). Similar migration barriers and a relative trend for Br diffusion have been reported by Meloni *et al.* in tetragonal $MAPbBr_3$.[68] These results suggest that Br diffusion in real crystals occurs both along apical and equatorial directions without having any preferential direction. Consequently,

the migration path with the higher activation energy, i.e., equatorial to apical hopping, can be considered as the rate limiting step for overall ion diffusion in this material (Figure S6). Therefore, in $MAPbBr_{3-x}Cl_x$ we calculate the activation energies of Br and Cl diffusion only along this high energy migration path. These simulations demonstrate two key results: (1) the activation energy for Cl (0.22-0.23 eV) is smaller than that for Br (0.47-0.59 eV) ions, (Figure S9 and Table S2) and (2) the migration barrier for Br markedly increases with the inclusion of Cl ions from 0.33 eV for $MAPbBr_3$ to 0.59 eV for $MAPbBr_{2.75}Cl_{0.25}$. Overall, the migration barrier for Br steadily raises with the Cl concentration in $MAPbBr_{3-x}Cl_x$, as shown in Figure 2a, Figure S6, and Table S2. This indicates limited interdiffusion of halogens as also reported for Cs-based perovskites.[47] Such change in ion dynamics can be rationalized by the fact that with the addition of smaller Cl ions effective lattice constant reduces. It follows the trend that the larger the anion size, the larger the anion migration barrier, as found by comparing iodide and bromide based perovskites.[68] Not surprisingly, due to its smaller ionic radii with respect to Br, the Cl diffusion barrier is lower in energy. Even though this indicates more pronounced Cl migration in the lattice, such enhanced ionic motion does not affect overall optoelectronic properties due to relatively low concentrations of Cl and reduced participation of Cl orbitals in near band-gap transitions as analyzed later.

To further investigate an increased Br migration barrier leading to partial suppression, of Br diffusion in $MAPbBr_{3-x}Cl_x$, we analyze the local structural distortions adjacent to the migration path of Br. As a characteristic measure of such distortions, we calculate the displacement of the neighboring Pb atom during Br migration. Larger displacements of Pb in $MAPbBr_{3-x}Cl_x$ compared to $MAPbBr_3$ demonstrate stronger geometric distortion in mixed-anion lattices (see Figure S8). As discussed earlier, Cl inclusion spatially contracts the lattice, narrowing the curved migration path for Br in these materials as shown in Figure S7.[65] This structural change and consequent steric constraints distort the local structure along the migration path of Br, increasing its activation energy. An increase in activation energy for Br with Cl concentration in the lattice further supports the link between volume contraction

and partially suppressed Br migration. Note that, similar limited halide interdiffusion in $MAPbI_{3-x}Br_x$ and $CsPbI_{3-x}Br_x$ in presence of Br anions in small concentration has been studied extensively.[47,69–71] For example, using a combination of experimental techniques, such as impedance spectroscopy and muon spin relaxation, Rodriguez *et al.* demonstrated largely suppressed iodide migration in $MAPbI_{2.5}Br_{0.5}$ due to the compact crystal structure of these mixed halide perovskites.[70]

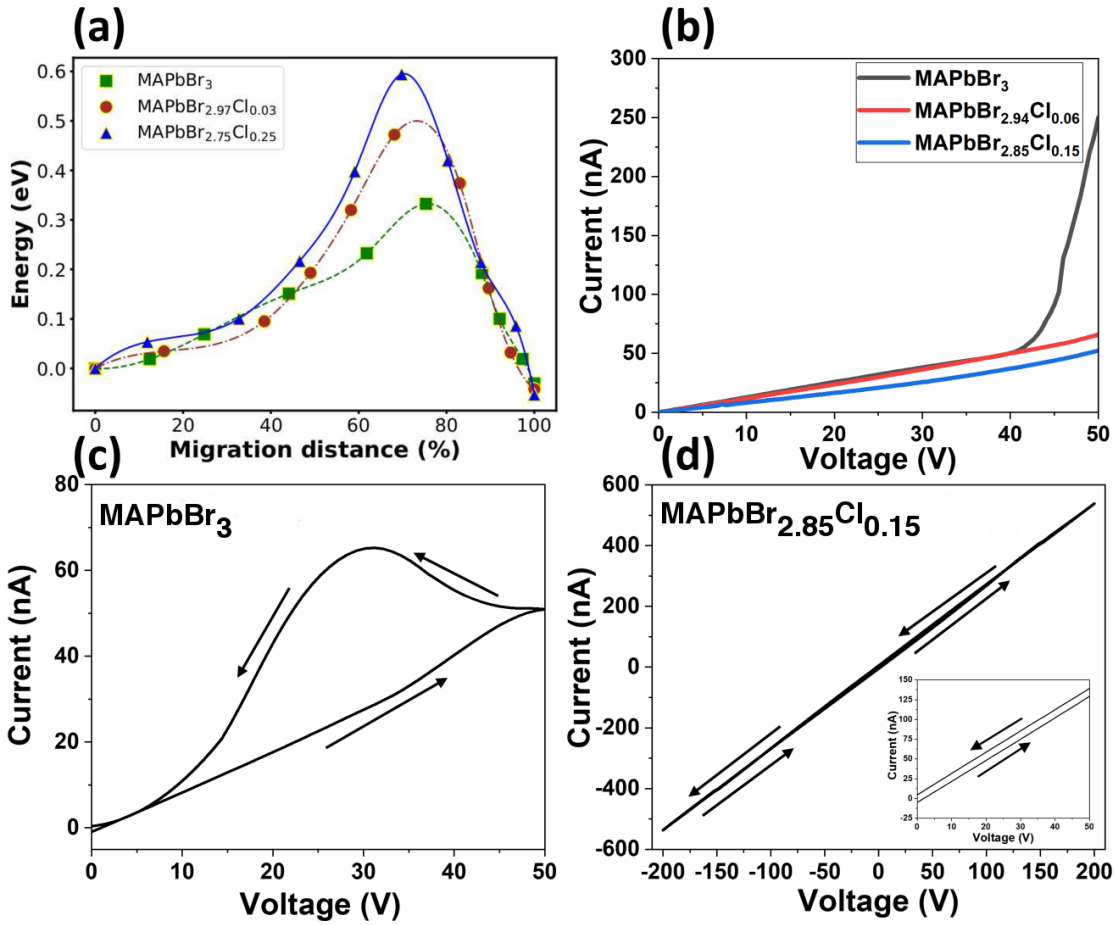

Figure 2: Ion migration in mixed halide perovskites.(a) Minimal energy path for Br ion migration in $MAPbBr_{3-x}Cl_x$ with different Cl concentration. (b) Dark current measurements for $MAPbBr_{3-x}Cl_x$ for small concentrations. (c) IV hysteresis loop for pure $Cr/MAPbBr_3/Cr$, as compared to the (d) negligible current hysteresis behavior shown for $Cr/MAPbBr_{2.85}Cl_{0.15}/Cr$ device.

To experimentally validate the partial suppression of Br ion migration in $MAPbBr_{3-x}Cl_x$, we measured the dark current at different Cl concentrations to indirectly probe ionic mo-

tion. The dark current for $MAPbBr_3$, $MAPbBr_{2.94}Cl_{0.06}$, and $MAPbBr_{2.85}Cl_{0.15}$ are shown in Figure 2b. The device architecture used for these measurements consisted of a simple metal/semiconductor/metal sandwich architecture, namely Cr/Perovskite/Cr. Cr contacts were used, as it has been shown that Cr contacts create an Ohmic contact between -20 to +20 V with $MAPbBr_3$.[72] This allowed for direct comparisons between device dark current and resistivity based on the results shown in Figure 2b. From 0 to +30V, the devices were fit with linear curves to calculate the low-bias-regime device resistivities. Five devices for each composition were measured to obtain an average resistivity (See Fig. S10). In this bias range, the resistivities of each of the five Cr/perovskite/Cr compositions were calculated (average of three detectors at each composition) as follows : $\rho_{MAPbBr_3} = 0.295 \pm 0.152$ GΩ.cm, $\rho_{MAPbBr_{2.94}Cl_{0.06}} = 0.745 \pm 0.352$ GΩ.cm, and $\rho_{MAPbBr_{2.85}Cl_{0.15}} = 1.522 \pm 0.156$ GΩ.cm. It is clear that incorporating small amounts of Cl into the $MAPbBr_3$ single crystals reduces the dark current, and causes an increase in resistivity, which is required to produce a high signal to noise ratio in applications requiring high bias, such as spectral resolution of γ-rays. We observe that the $MAPbBr_3$ device has a turn on voltage of around +40 V with large hysteretic behavior, as shown in Figures 2b. Figure 2c was measured with a separate $MAPbBr_3$ device to show the large variation that exists among different $MAPbBr_3$ devices. Meanwhile, there is less variation in the Cl-doped crystals, which alludes to more controlled, consistent, high-quality growth for small amounts of Cl-doping. Also, the characteristics for Cl-doped samples stay linear with no signs of severe hysteresis when measured at the same scan speed. This indicates that ion migration is partially suppressed in the Cl-doped $MAPbBr_3$ single crystals, as current-voltage hysteresis in hybrid perovskite materials has been directly linked to ion migration.[61] To further demonstrate the partial suppression of ion migration, the $MAPbBr_{2.85}Cl_{0.15}$ based device was scanned in a loop IV curve, as shown in Figure 2d. This device has minimal hysteresis from -200 V to +200 V, and also shows symmetric negative and positive IV behavior, where we observe a consistent absolute value of current around 540 nA at a bias of ± 200 V. The inset of Figure 2d shows a zoomed-in portion of the IV

curve to compare the $MAPbBr_3$ to the $MAPbBr_{2.85}Cl_{0.15}$ device. Note that, in Figure 2b we used the forward scans to compare device resistivity among the 0, 2, and 5% Cl-incorporated single crystals. In Figures 2c,d, we aimed to probe the hysteretic behavior of the devices to further understand the properties of the 0, 2, and 5% single crystalline devices. It is clearly seen that there is a minimal hysteresis in the Cl-doped device, as compared to the pure $MAPbBr_3$ device. This alludes to the fact that the halide mixing in $MAPbBr_{3-x}Cl_x$ single crystals partially suppresses ion migration, leading towards more stable response with negligible hysteresis at large electric fields required for γ-ray spectroscopy.

To further understand the effect of Cl incorporation on the electronic structure, we analyzed the partial density of states for $MAPbBr_{3-x}Cl_x$ with HSE06+SOC based DFT simulations. As shown in Figures 3a,b and S11,12, the valence band predominantly forms from 4p Br and 6s Pb, whereas 6p Pb mainly contributes to the conduction band edge. We find a very small contribution from the Cl orbitals to both the valence band (VB) and the conduction band (CB) edges of these mixed-halide perovskites (Figure S11). Thus, as also shown in Figure 3a and 3b, the delocalized charge density of the VB over the entire Pb-Br framework in $MAPbBr_3$ becomes partially localized in $MAPbBr_{3-x}Cl_x$ due to the negligible participation of Cl atoms. The localization of the VB charge density upon Cl incorporation can be clearly seen from the plotted band decomposed charge density in Figure 3b. On the contrary, as the CB wave function is dominantly localized over the Pb atoms (Figure S12), it remains mostly unchanged with anion mixing in these materials.

Predicted significant influence of Cl mixing on the charge density of the frontier bands further directs us to investigate the charge carrier transport in $MAPbBr_{3-x}Cl_x$ by calculating the effective masses (m*). Under a constant relaxation-time (τ) approximation, carrier mobilities inversely vary with these effective masses according to the relation, $\mu = e\tau/m^*$, where e is elementary charge. For $MAPbBr_3$, we evaluate small electron and hole effective masses to be 0.17 and 0.20, (in units of electron mass) respectively, which agrees well with previous experimental and computational reports.[73,74] Moreover, as shown in Figure 3c, the

carrier effective masses reduce moderately with increased Cl concentration in $MAPbBr_{3-x}Cl_x$, indicating enhanced carrier mobilities in these crystals. Previous experiments have also reported enhanced carrier transport behavior with Br/Cl mixing in halide perovskites.[18] The almost equal effective masses for electrons and holes in these materials also indicates a more balanced charge carrier transport character which is highly desired for efficient γ-ray detector semiconductors.

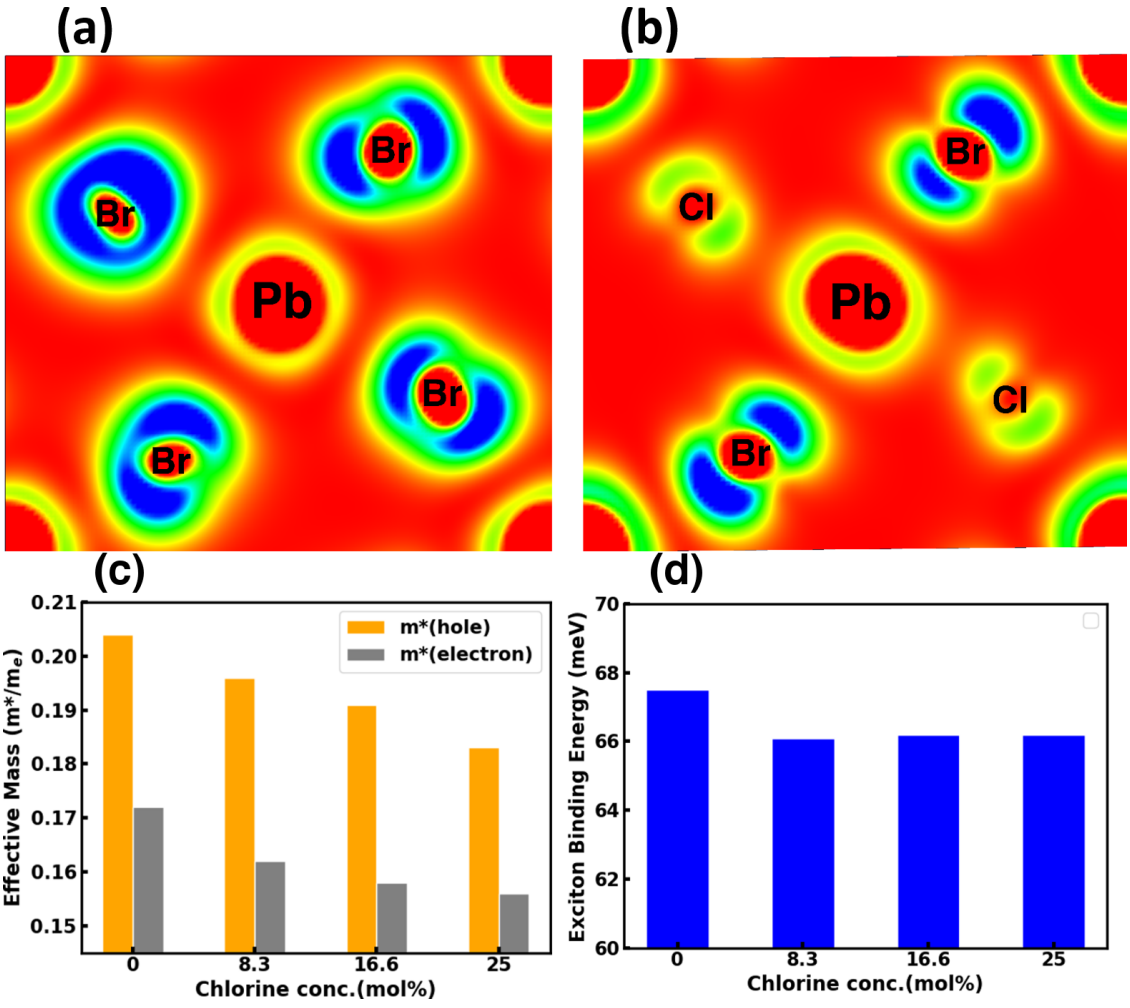

Figure 3: Effect of anion mixing in the electronic properties of $MAPbBr_{3-x}Cl_x$ with HSE06+SOC based DFT simulations. Band decomposed charge density for VBM in (a) $MAPbBr_3$ and (b) $MAPbBr_{2.25}Cl_{0.75}$. Color scale for: red is defined as 0 and blue as 0.00025 eÅ^{-3}. The change in (c) effective masses and (d) exciton binding energies with Cl incorporation.

Recent studies have also identified that the presence of excitons significantly influences

the photophysical properties of bromide and chloride based perovskites.[73,75,76] Higher exciton binding energies significantly hinders the free charge-carrier generation, ultimately reducing the carrier transport of a photovoltaic material.[77] Furthermore, experimental reports indicate increased exciton binding energies for bromide and chloride based hybrid perovskites compared to that for the iodide one.[73,78,79] So, the effect of Cl inclusion on the excitonic behavior is important to understand the optoelectronics of $MAPbBr_{3-x}Cl_x$. We computationally evaluate the exciton binding energies (details of calculation are included in Methods section) for these mixed halide perovskites as shown in Figure 3d. As discussed in previous studies, we considered the excitons as the Mott-Wannier type for which the effective Bohr diameter is much larger than the host lattice constant.[12,80] Within this model, we calculate the exciton binding energy as 67 meV for $MAPbBr_3$, agreeing very well with previous optical absorption and magneto-absorption based experimental reports.[81,82] Further exploring mixed halide perovskites, the binding energies are found to be very similar for all $MAPbBr_{3-x}Cl_x$, depicting negligible effects of Cl mixing towards the excitonic nature of these lattices. Simultaneous lowering of reduced effective masses and a high-frequency dielectric constant (see Figure S12) makes the exciton binding energy mostly insensitive to the anion mixing in these perovskites. Thus, our study indicates that Cl inclusion does not affect the excitonic nature of the charge carrier transport in these halide perovskites.

Finally, we demonstrate the importance of Cl incorporation in the $MAPbBr_3$ perovskite single crystals in regards to high-energy γ-ray radiation detection (Figures 4a-c). We fabricated devices with a structure of $Cr/MAPbBr_{3-x}Cl_x/Cr$ to test for γ-ray responses. Ten different devices were tested using pure $MAPbBr_3$ as the radiation absorbing semiconductor single crystal. When exposed to ^{241}Am source, all of the devices showed no appreciable pulses above the baseline on the oscilloscope. This may be due to the lower resistivity of $MAPbBr_3$, where the noise to signal ratio is too low to resolve γ-rays. However, with $MAPbBr_{2.85}Cl_{0.15}$ based devices, we observed many clear pulses. Figures 4b and 4c show two of the analyzed pulses obtained from $MAPbBr_{2.85}Cl_{0.15}$. Note that we use $MAPbBr_{2.85}Cl_{0.15}$ for γ-ray detec-

tion as this composition results in the lowest dark current. Here, we observe that increasing the electric field through the device results in a larger pulse/signal amplitude and faster rise time (represented as 10% to 90% of the rise in the pulse), as expected. At room temperature, after counting for 5 minutes, the spectrum for ^{241}Am source was collected as shown in Figure 4a, with a spectral resolution of 35%. While the resolution of the photopeak is low, it is in agreement with previous reports exploring other hybrid perovskite compositions.[83,84]

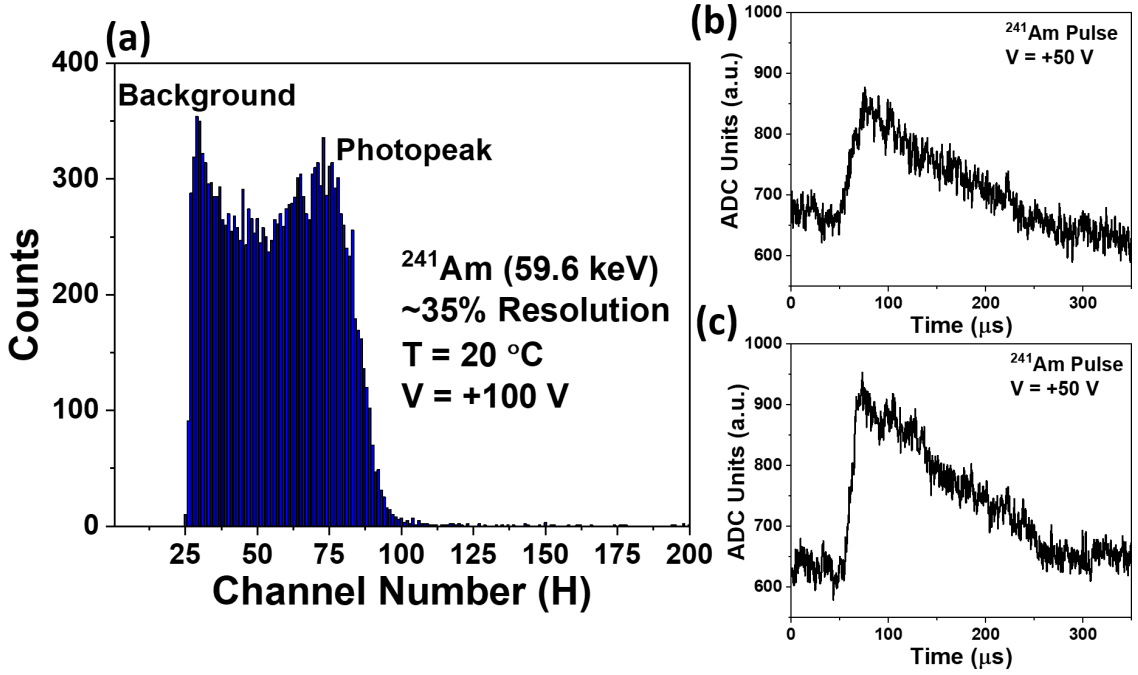

Figure 4: (a) Energy resolved spectrum of 59.6 keV-rays from a ^{241}Am source using a Cr/$MAPbBr_{2.85}Cl_{0.15}$/Cr device structure. (b,c) ADC (analog to digital converter) traces of pulses obtained from single photon counting with the device from ^{241}Am. Both pulses recorded at room temperature, with a bias of +50 V and +100V, respectively.

For a halide perovskite based γ-ray detector, the presence of high dark current, particularly under high electric field, strongly introduces electronic noise which adversely affects the resolution of the semiconductor detector. We find that ion-migration mediated dark current can be strongly suppressed by controlled anion mixing in $MAPbBr_{3-x}Cl_x$, consequently reducing electronic noise in the device and resulting in a prominent γ-ray spectrum for ^{241}Am. Enhanced and more balanced charge carrier transport is another influential factor for these detectors, as it ensures efficient charge collection in the devices. An overall increase of the car-

rier mobilities in $MAPbBr_{3-x}Cl_x$, indicated by decreasing effective masses as a function of Cl concentration, depicts improved carrier transport in these materials. Improvement in the signal to noise ratio, increase in device resistivity, and enhanced and balanced charge transport due to anion mixing, are a few of the major influences on strong γ-ray radiation response in these $MAPbBr_{3-x}Cl_x$ perovskite single crystals. With three $Cr/MAPbBr_{2.85}Cl_{0.15}/Cr$ working devices, we tested the response to ^{241}Am photons on a regular basis once a week to get a general idea of the device stability. In these experiments, no degradation was readily visible as the strong response and signal to noise ratio was observable every measurement for 8 to 12 weeks. Each time the devices were stored in the dark (inside a laboratory drawer). After this time period, devices stopped responding to γ-ray photons, possibly due to material degradation. We plan to conduct follow up studies to more deeply understand the device stability and what types of degradation cause instabilities over time.

In conclusion, anion-mixing in single crystal growth of the $MAPbBr_{3-x}Cl_x$ hybrid perovskite is an efficient and simple synthetic route of tuning optoelectronic properties of these materials. In this work, our combined experimental and computational techniques bring detailed information on how anion mixing affects physical processes related to high energy radiation detection across multiple length-scales. Incorporation of Cl is homogeneous in the bulk of $MAPbBr_{3-x}Cl_x$. In particular, we demonstrate that this processes efficiently suppress Br ion migration. Reduced effective carrier masses and almost unaffected exciton binding energies further underpin enhanced optoelectronic properties for these Cl-mixed perovskites. These improved properties result in a prominent increase in γ-ray detection ability for $MAPbBr_{3-x}Cl_x$ compared to pristine $MAPbBr_3$. Therefore, this study provides a deep atomistic understanding of the effects of anion mixing in hybrid perovskites, and suggests materials design strategies to enhance high-energy radiation detection using these materials.

Methods

Computational Details

Geometry relaxation and electronic structure calculations were performed within density functional theory (DFT)-based simulations as implemented in the Vienna Ab Initio Simulation Package (VASP).[85,86] The projected augmented wave (PAW) method, Van der Waals correction as described by Grimme and generalized gradient approximation (GGA) with the Perdew-Burke-Ernzerhof functional (PBE) for the exchange and correlation interactions have been considered.[87–89] To compute the impact of Cl inclusion with experimental concentrations of as low as 2% to the crystal structure, a large 2×2×1 supercell (16 formula unit) of the parent $MAPbBr_3$ was considered. Unit cell (4 formula units) of orthorhombic $MAPbBr_3$ which is stable at low temperature has been considered as the parent system for all the electronic structure simulations. Note that, as orthorhombic $MAPbBr_3$ shows dynamical stability, we considered this phase for all our simulations.[90] Structure optimization is considered to be converged when the maximum residual force on each atom becomes smaller than 0.01 eV/Å. Self-consistent calculations for electronic structure calculations are performed including spin-orbit coupling corrections and considering screened hybrid functionals of Heyd-Scuseria-Ernzerhof (HSE06) unless otherwise stated. The Brillouin-zones are sampled with 4×4×4 and 2×2×2 Monkhorst-Pack k-point mesh for geometry optimization and HSE06-SOC based self-consistent calculations, respectively. Details of Helmholtz Free Energy calculations are described in SI (Section S1). The carrier effective masses were calculated using least-squares fit for parabolic band dispersion.[91] The high-frequency dielectric constants were evaluated within independent particle approximation. Activation energies for ion transport processes were evaluated from the total energy difference between the diffusing anions (i.e. Br or Cl) in their ground-state configuration and at the saddle point of the hopping process. For these simulations, we considered very large 2×2×2 supercell (32 formula units) to ensure that ion migration path does not get influenced by the spurious

periodic defect images. Here ion diffusion has been modeled by single-hopping of ions to the nearest ion vacancy site inside the supercell. Climbing-image nudged elastic band (CI-NEB) methodology as implemented by Henkelman has been used to determine the minimum energy path (MEP) for the ion transport.[66] Ten images were considered along the MEP to model the migration path accurately enough.

We further evaluate the exciton binding energy (E_b) that measures strength of the Coulombic attraction in the photogenerated electron-hole pair. For 3-dimensional halide perovskites, the excitons are mostly identified as the Wannier-Mott type where electron-hole binding is weak and electron and hole densities are spatially delocalized.[80] From the effective mass theory,[92] the effective Bohr diameter of such an exciton can be estimated as,

$$a_0 = 2\hbar^2\epsilon^\infty/(e^2\mu) \tag{1}$$

where μ is the reduced carrier mass and ϵ^∞ is the effective dielectric constant at infinite frequency. Empirical formula using the effective masses and dielectric constants further define the binding energy of electron-hole pair in an exciton as follows,

$$E_\mathrm{b} = 2\hbar^2/(\mu {a_0}^2) \tag{2}$$

Details of the Wannier-Mott type exciton in halide perovskites has been extensively discussed by Manser *et al.*[80]

Experimental Procedure

Growth of $MAPbBr_{3-x}Cl_x$ Single Crystals

$MAPbBr_{3-x}Cl_x$ single crystals were grown using the inverse temperature crystallization technique. All materials used for single crystal growth were purchased and used as-received including: N,N-Dimethylformamide (DMF) (Sigma Aldrich, anhydrous, 99.8%), PbBr2 (Alfa

Aesar, Puratronic, 99.998%, metals basis), MABr (GreatCell Solar, >99%), MACl (EMD Millipore, >99.0%). Solutions were prepared using a 1:1 molar ratio of Pb precursor to organic precursors. To obtain a specific percentage of Cl inclusion in solution, the organic precursors (MABr and MACl) were calculated and measured for 0%, 2%, 5%, 10%, 15%, and 20 mol% Cl in the prepared single crystal growth solutions. Here, the organic precursor was used for Cl inclusion in solution due to higher solubility in the $MAPbBr_{3-x}Cl_x$ solution. Each solution was stirred for two hours at room temperature until completely dissolved. The solutions were then filtered using 0.45 μm PTFE filters and separated into scintillation vials with 2 mL each. The vials were then placed in an oil bath on a hot plate and heated to ≈80°C for final crystallization.

Structural and Optical Characterization

All experimental measurements were completed on single crystals, as grown. No post-growth treatments were utilized. Single crystals were ground into fine powders, and Powder XRD was used to characterize the lattice parameter of each Cl-dopant concentration. The Powder XRD measurements were completed using a Rigaku Ultima III. JADE software was used for Rietveld refinements for lattice parameters using the $Pm\bar{3}m$ .cif file for $CH_3NH_3PbBr_3$ received from the crystallography open database (COD ID 1545320). Optical measurements included UV-Vis absorption and photoluminescence. UV-Vis absorption spectra were taken for each of the five different compositions of $MAPbBr_{3-x}Cl_x$ listed above using transmission mode, then converted to Tauc plots to determine the band gap for each single crystal composition. Three separate crystals from each composition were tested for statistical analysis of the compositional band gaps. For photoluminescence measurements, the same three crystals were tested for each composition. Three different spots on each of the three crystals per composition were measured for statistical analysis of PL, to understand the uniformity of the surfaces of each single crystalline composition. Radiation measurements were performed in an aluminum light-sealed box to reduce the effect of noise from light-interactions with the crystals. Here, we used a Keithley 6847 HV power supply, an

Ortec 142PC preamplifier with an Ortec 4002P preamp power supply, a low noise preamplifier filter SR560 (Stanford Research Systems), and a Tektronix PPO 4104 digital phosphor oscilloscope. For spectra collection, we used an Ortec Dspec-Pro MCA paired with Maestro v7.01 from Ortec.

Acknowledgement

The work at Los Alamos National Laboratory (LANL) was supported by the LANL Laboratory Directed Research and Development Funds (LDRD) program. This work was done in part at the Center for Nonlinear Studies (CNLS) and the Center for Integrated Nanotechnologies (CINT), a U.S. Department of Energy and Office of Basic Energy Sciences user facility, at LANL. This research used resources provided by the LANL Institutional Computing Program. Los Alamos National Laboratory is operated by Triad National Security, LLC, for the National Nuclear Security Administration of the U.S. Department of Energy (Contract No. 89233218NCA000001). J.E. acknowledges the Institut Universitaire de France.

Supporting Information Available

Electronic Supplementary Information (ESI) available: lattice parameter and structural changes in $MAPbBr_{3-x}Cl_x$ with Cl incorporation, changes in electronic and optical properties, energy barriers of Br/Cl ion migration in the lattice, details of Helmholtz free energy. This material is available free of charge via the Internet at `http://pubs.acs.org/`.

References

(1) Kojima, A.; Teshima, K.; Shirai, Y.; Miyasaka, T. Organometal Halide Perovskites as Visible-light Sensitizers for Photovoltaic Cells. *J. Am. Chem. Soc.* **2009**, *131*, 6050–

6051.

(2) Lee, M. M.; Teuscher, J.; Miyasaka, T.; Murakami, T. N.; Snaith, H. J. Efficient Hybrid Solar Cells Based on Meso-superstructured Organometal Halide Perovskites. *Science* **2012**, *338*, 643–647.

(3) Green, M. A.; Ho-Baillie, A.; Snaith, H. J. The Emergence of Perovskite Solar Cells. *Nat. Photonics* **2014**, *8*, 506–514.

(4) Grätzel, M. The Light and Shade of Perovskite Solar Cells. *Nat. Mater.* **2014**, *13*, 838–842.

(5) Dou, L.; Yang, Y. M.; You, J.; Hong, Z.; Chang, W.-H.; Li, G.; Yang, Y. Solution-processed hybrid perovskite photodetectors with high detectivity. *Nat. Commun.* **2014**, *5*, 5404.

(6) Snaith, H. J. Present status and future prospects of perovskite photovoltaics. *Nat. Mater.* **2018**, *17*, 372.

(7) Jena, A. K.; Kulkarni, A.; Miyasaka, T. Halide perovskite photovoltaics: background, status, and future prospects. *Chem. Rev.* **2019**, *119*, 3036–3103.

(8) Fang, Y.; Dong, Q.; Shao, Y.; Yuan, Y.; Huang, J. Highly narrowband perovskite single-crystal photodetectors enabled by surface-charge recombination. *Nat. Photonics* **2015**, *9*, 679.

(9) Tan, Z.-K.; Moghaddam, R. S.; Lai, M. L.; Docampo, P.; Higler, R.; Deschler, F.; Price, M.; Sadhanala, A.; Pazos, L. M.; Credgington, D. Bright light-emitting diodes based on organometal halide perovskite. *Nat. Nanotechnol* **2014**, *9*, 687.

(10) Yuan, M.; Quan, L. N.; Comin, R.; Walters, G.; Sabatini, R.; Voznyy, O.; Hoogland, S.; Zhao, Y.; Beauregard, E. M.; Kanjanaboos, P. Perovskite energy funnels for efficient light-emitting diodes. *Nat. Nanotechnol* **2016**, *11*, 872.

(11) Stranks, S. D.; Eperon, G. E.; Grancini, G.; Menelaou, C.; Alcocer, M. J.; Leijtens, T.; Herz, L. M.; Petrozza, A.; Snaith, H. J. Electron-hole diffusion lengths exceeding 1 micrometer in an organometal trihalide perovskite absorber. *Science* **2013**, *342*, 341–344.

(12) Protesescu, L.; Yakunin, S.; Bodnarchuk, M. I.; Krieg, F.; Caputo, R.; Hendon, C. H.; Yang, R. X.; Walsh, A.; Kovalenko, M. V. Nanocrystals of cesium lead halide perovskites (CsPbX3, X= Cl, Br, and I): novel optoelectronic materials showing bright emission with wide color gamut. *Nano Lett* **2015**, *15*, 3692–3696.

(13) Meggiolaro, D.; De Angelis, F. First-Principles Modeling of Defects in Lead Halide Perovskites: Best Practices and Open Issues. *ACS Energy Lett* **2018**, *3*, 2206–2222.

(14) Pan, W.; Wu, H.; Luo, J.; Deng, Z.; Ge, C.; Chen, C.; Jiang, X.; Yin, W.-J.; Niu, G.; Zhu, L. Cs 2 AgBiBr 6 single-crystal X-ray detectors with a low detection limit. *Nat. Photonics* **2017**, *11*, 726.

(15) He, Y.; Matei, L.; Jung, H. J.; McCall, K. M.; Chen, M.; Stoumpos, C. C.; Liu, Z.; Peters, J. A.; Chung, D. Y.; Wessels, B. W. High spectral resolution of gamma-rays at room temperature by perovskite CsPbBr 3 single crystals. *Nat. Commun.* **2018**, *9*, 1609.

(16) Wei, H.; Huang, J. Halide lead perovskites for ionizing radiation detection. *Nat. Commun.* **2019**, *10*, 1066.

(17) Chen, Q.; Wu, J.; Ou, X.; Huang, B.; Almutlaq, J.; Zhumekenov, A. A.; Guan, X.; Han, S.; Liang, L.; Yi, Z. All-inorganic perovskite nanocrystal scintillators. *Nature* **2018**, *561*, 88.

(18) Wei, H.; DeSantis, D.; Wei, W.; Deng, Y.; Guo, D.; Savenije, T. J.; Cao, L.; Huang, J. Dopant compensation in alloyed CH 3 NH 3 PbBr 3- x Cl x perovskite single crystals for gamma-ray spectroscopy. *Nat. Mater.* **2017**, *16*, 826.

(19) Saliba, M.; Matsui, T.; Seo, J.-Y.; Domanski, K.; Correa-Baena, J.-P.; Mohammad K., N.; Zakeeruddin, S. M.; Tress, W.; Abate, A.; Hagfeldt, A.; Grätzel, M. Cesium-containing Triple Cation Perovskite Solar Cells: Improved Stability, Reproducibility and High Efficiency. *Energy Environ. Sci.* **2016**, *9*, 1989–1997.

(20) McMeekin, D. P.; Sadoughi, G.; Rehman, W.; Eperon, G. E.; Saliba, M.; Hörantner, M. T.; Haghighirad, A.; Sakai, N.; Korte, L.; Rech, B.; Johnston, M. B.; Herz, L. M.; Snaith, H. J. A Mixed-cation Lead Mixed-halide Perovskite Absorber for Tandem Solar Cells. *Science* **2016**, *351*, 151–155.

(21) Ghosh, D.; Smith, A. R.; Walker, A. B.; Islam, M. S. Mixed A-Cation Perovskites for Solar Cells: Atomic-Scale Insights Into Structural Distortion, Hydrogen Bonding, and Electronic Properties. *Chem. Mater.* **2018**, *30*, 5194–5204.

(22) Jaffe, A.; Lin, Y.; Karunadasa, H. I. Halide Perovskites Under Pressure: Accessing New Properties Through Lattice Compression. *ACS Energy Lett.* **2017**, *2*, 1549–1555.

(23) Kong, L.; Liu, G.; Gong, J.; Hu, Q.; Schaller, R. D.; Dera, P.; Zhang, D.; Liu, Z.; Yang, W.; Zhu, K. Simultaneous band-gap narrowing and carrier-lifetime prolongation of organic–inorganic trihalide perovskites. *Proc. Natl. Acad. Sci.* **2016**, *113*, 8910–8915.

(24) Zhang, X.; Li, L.; Sun, Z.; Luo, J. Rational chemical doping of metal halide perovskites. *Chem. Soc. Rev.* **2019**, *48*, 517–539.

(25) Ghosh, D.; Walsh Atkins, P.; Islam, M. S.; Walker, A. B.; Eames, C. Good Vibrations: Locking of Octahedral Tilting in Mixed-Cation Iodide Perovskites for Solar Cells. *ACS Energy Lett.* **2017**, *2*, 2424–2429.

(26) Nagane, S.; Ghosh, D.; Hoye, R. L.; Zhao, B.; Ahmad, S.; Walker, A. B.; Islam, M. S.; Ogale, S.; Sadhanala, A. Lead-Free Perovskite Semiconductors Based on Germanium–Tin Solid Solutions: Structural and Optoelectronic Properties. *J. Phys. Chem. C* **2018**, *122*, 5940–5947.

(27) Ghosh, D.; Aziz, A.; Dawson, J. A.; Walker, A. B.; Islam, M. S. Putting the Squeeze on Lead Iodide Perovskites: Pressure-Induced Effects to Tune their Structural and Optoelectronic Behaviour. *Chem. Mater* **2019**, *31*, 4063.

(28) Xing, G.; Mathews, N.; Sun, S.; Lim, S. S.; Lam, Y. M.; Grätzel, M.; Mhaisalkar, S.; Sum, T. C. Long-range balanced electron-and hole-transport lengths in organic-inorganic $CH_3NH_3PbI_3$. *Science* **2013**, *342*, 344–347.

(29) Chen, Q.; Zhou, H.; Fang, Y.; Stieg, A. Z.; Song, T.-B.; Wang, H.-H.; Xu, X.; Liu, Y.; Lu, S.; You, J. The optoelectronic role of chlorine in CH 3 NH 3 PbI 3 (Cl)-based perovskite solar cells. *Nat. Commun.* **2015**, *6*, 7269.

(30) Yantara, N.; Yanan, F.; Shi, C.; Dewi, H. A.; Boix, P. P.; Mhaisalkar, S. G.; Mathews, N. Unravelling the effects of Cl addition in single step CH3NH3PbI3 perovskite solar cells. *Chem. Mater.* **2015**, *27*, 2309–2314.

(31) Nie, W.; Tsai, H.; Asadpour, R.; Blancon, J.-C.; Neukirch, A. J.; Gupta, G.; Crochet, J. J.; Chhowalla, M.; Tretiak, S.; Alam, M. A. High-efficiency solution-processed perovskite solar cells with millimeter-scale grains. *Science* **2015**, *347*, 522–525.

(32) Yang, B.; Keum, J.; Ovchinnikova, O. S.; Belianinov, A.; Chen, S.; Du, M.-H.; Ivanov, I. N.; Rouleau, C. M.; Geohegan, D. B.; Xiao, K. Deciphering halogen competition in organometallic halide perovskite growth. *J. Am. Chem. Soc.* **2016**, *138*, 5028–5035.

(33) Dar, M. I.; Arora, N.; Gao, P.; Ahmad, S.; Gratzel, M.; Nazeeruddin, M. K. Investigation regarding the role of chloride in organic–inorganic halide perovskites obtained from chloride containing precursors. *Nano Lett* **2014**, *14*, 6991–6996.

(34) Tidhar, Y.; Edri, E.; Weissman, H.; Zohar, D.; Hodes, G.; Cahen, D.; Rybtchinski, B.; Kirmayer, S. Crystallization of methyl ammonium lead halide perovskites: implications for photovoltaic applications. *J. Am. Chem. Soc.* **2014**, *136*, 13249–13256.

(35) Zhang, M.; Yu, H.; Lyu, M.; Wang, Q.; Yun, J.-H.; Wang, L. Composition-dependent photoluminescence intensity and prolonged recombination lifetime of perovskite CH 3 NH 3 PbBr 3- x Cl x films. *Chem Commun* **2014**, *50*, 11727–11730.

(36) Wei, M.; Chung, Y.-H.; Xiao, Y.; Chen, Z. Color tunable halide perovskite CH3NH3PbBr3- xClx emission via annealing. *Org Electron.* **2015**, *26*, 260–264.

(37) Edri, E.; Kirmayer, S.; Kulbak, M.; Hodes, G.; Cahen, D. Chloride inclusion and hole transport material doping to improve methyl ammonium lead bromide perovskite-based high open-circuit voltage solar cells. *J. Phys. Chem. Lett* **2014**, *5*, 429–433.

(38) Zhang, F.; Zhong, H.; Chen, C.; Wu, X.-g.; Hu, X.; Huang, H.; Han, J.; Zou, B.; Dong, Y. Brightly luminescent and color-tunable colloidal CH3NH3PbX3 (X= Br, I, Cl) quantum dots: potential alternatives for display technology. *ACS Nano* **2015**, *9*, 4533–4542.

(39) Kim, Y.-H.; Cho, H.; Heo, J. H.; Kim, T.-S.; Myoung, N.; Lee, C.-L.; Im, S. H.; Lee, T.-W. Multicolored organic/inorganic hybrid perovskite light-emitting diodes. *Adv. Mater.* **2015**, *27*, 1248–1254.

(40) Tisdale, J. T.; Smith, T.; Salasin, J. R.; Ahmadi, M.; Johnson, N.; Ievlev, A. V.; Koehler, M.; Rawn, C. J.; Lukosi, E.; Hu, B. Precursor purity effects on solution-based growth of MAPbBr 3 single crystals towards efficient radiation sensing. *CrystEngComm* **2018**, *20*, 7818–7825.

(41) Xu, Q.; Wei, H.; Wei, W.; Chuirazzi, W.; DeSantis, D.; Huang, J.; Cao, L. Detection of charged particles with a methylammonium lead tribromide perovskite single crystal. *Nuclear Instruments and Methods in Physics Research Section A: Accelerators, Spectrometers, Detectors and Associated Equipment* **2017**, *848*, 106–108.

(42) He, Y.; Ke, W.; Alexander, G. C.; McCall, K. M.; Chica, D. G.; Liu, Z.; Hadar, I.;

Stoumpos, C. C.; Wessels, B. W.; Kanatzidis, M. G. Resolving the Energy of γ-Ray Photons with MAPbI3 Single Crystals. *ACS Photonics* **2018**, *5*, 4132–4138.

(43) Lukosi, E.; Smith, T.; Tisdale, J.; Hamm, D.; Seal, C.; Hu, B.; Ahmadi, M. Methylammonium lead tribromide semiconductors: Ionizing radiation detection and electronic properties. *Nuclear Instruments and Methods in Physics Research Section A: Accelerators, Spectrometers, Detectors and Associated Equipment* **2019**, *927*, 401–406.

(44) Kim, S.-Y.; Lee, H.-C.; Nam, Y.; Yun, Y.; Lee, S.-H.; Kim, D. H.; Noh, J. H.; Lee, J.-H.; Kim, D.-H.; Lee, S. Ternary diagrams of the phase, optical bandgap energy and photoluminescence of mixed-halide perovskites. *Acta Mater.* **2019**, *181*, 460–469.

(45) Rosales, B. A.; Men, L.; Cady, S. D.; Hanrahan, M. P.; Rossini, A. J.; Vela, J. Persistent dopants and phase segregation in organolead mixed-halide perovskites. *Chem. Mater.* **2016**, *28*, 6848–6859.

(46) Bischak, C. G.; Hetherington, C. L.; Wu, H.; Aloni, S.; Ogletree, D. F.; Limmer, D. T.; Ginsberg, N. S. Origin of reversible photoinduced phase separation in hybrid perovskites. *Nano Lett* **2017**, *17*, 1028–1033.

(47) Pan, D.; Fu, Y.; Chen, J.; Czech, K. J.; Wright, J. C.; Jin, S. Visualization and studies of ion-diffusion kinetics in cesium lead bromide perovskite nanowires. *Nano Lett.* **2018**, *18*, 1807–1813.

(48) Jang, D. M.; Park, K.; Kim, D. H.; Park, J.; Shojaei, F.; Kang, H. S.; Ahn, J.-P.; Lee, J. W.; Song, J. K. Reversible halide exchange reaction of organometal trihalide perovskite colloidal nanocrystals for full-range band gap tuning. *Nano Lett.* **2015**, *15*, 5191–5199.

(49) Yin, W.-J.; Yan, Y.; Wei, S.-H. Anomalous alloy properties in mixed halide perovskites. *J. Phys. Chem. Lett* **2014**, *5*, 3625–3631.

(50) Brivio, F.; Caetano, C.; Walsh, A. Thermodynamic origin of photoinstability in the CH3NH3Pb (I1–x Br x) 3 hybrid halide perovskite alloy. *J. Phys. Chem. Lett.* **2016**, *7*, 1083–1087.

(51) Chen, T.; Foley, B. J.; Park, C.; Brown, C. M.; Harriger, L. W.; Lee, J.; Ruff, J.; Yoon, M.; Choi, J. J.; Lee, S.-H. Entropy-driven Structural Transition and Kinetic Trapping in Formamidinium Lead Iodide Perovskite. *Sci. Adv.* **2016**, *2*, e1601650.

(52) Noh, J. H.; Im, S. H.; Heo, J. H.; Mandal, T. N.; Seok, S. I. Chemical management for colorful, efficient, and stable inorganic–organic hybrid nanostructured solar cells. *Nano Lett.* **2013**, *13*, 1764–1769.

(53) Comin, R.; Walters, G.; Thibau, E. S.; Voznyy, O.; Lu, Z.-H.; Sargent, E. H. Structural, optical, and electronic studies of wide-bandgap lead halide perovskites. *J. Mater. Chem. C* **2015**, *3*, 8839–8843.

(54) Sadhanala, A.; Ahmad, S.; Zhao, B.; Giesbrecht, N.; Pearce, P. M.; Deschler, F.; Hoye, R. L.; Godel, K. C.; Bein, T.; Docampo, P. Blue-green color tunable solution processable organolead chloride–bromide mixed halide perovskites for optoelectronic applications. *Nano Lett.* **2015**, *15*, 6095–6101.

(55) Zhang, T.; Yang, M.; Benson, E. E.; Li, Z.; van de Lagemaat, J.; Luther, J. M.; Yan, Y.; Zhu, K.; Zhao, Y. A facile solvothermal growth of single crystal mixed halide perovskite CH 3 NH 3 Pb (Br 1- x Cl x) 3. *Chem. Commun.* **2015**, *51*, 7820–7823.

(56) Menéndez-Proupin, E.; Palacios, P.; Wahnón, P.; Conesa, J. Self-consistent relativistic band structure of the CH 3 NH 3 PbI 3 perovskite. *Phys Rev B* **2014**, *90*, 045207.

(57) Even, J.; Pedesseau, L.; Jancu, J.-M.; Katan, C. Importance of spin–orbit coupling in hybrid organic/inorganic perovskites for photovoltaic applications. *J. Phys. Chem. Lett* **2013**, *4*, 2999–3005.

(58) Bandiello, E.; Ávila, J.; Gil-Escrig, L.; Tekelenburg, E.; Sessolo, M.; Bolink, H. J. Influence of Mobile Ions on the Electroluminescence Characteristics of Methylammonium Lead Iodide Perovskite Diodes. *J. Mater. Chem. A* **2016**, *4*, 18614–18620.

(59) Frost, J. M.; Walsh, A. What Is Moving in Hybrid Halide Perovskite Solar Cells? *Acc. Chem. Res.* **2016**, *49*, 528–535.

(60) Yuan, Y.; Huang, J. Ion migration in organometal trihalide perovskite and its impact on photovoltaic efficiency and stability. *Acc. Chem. Res* **2016**, *49*, 286–293.

(61) Snaith, H. J.; Abate, A.; Ball, J. M.; Eperon, G. E.; Leijtens, T.; Noel, N. K.; Stranks, S. D.; Wang, J. T.-W.; Wojciechowski, a.; et., Anomalous Hysteresis in Perovskite Solar Cells. *J. Phys. Chem. Lett.* **2014**, *5*, 1511–1515.

(62) Xiao, Z.; Yuan, Y.; Shao, Y.; Wang, Q.; Dong, Q.; Bi, C.; Sharma, P.; Gruverman, A.; Huang, J. Giant switchable photovoltaic effect in organometal trihalide perovskite devices. *Nat. Mater.* **2015**, *14*, 193–198.

(63) Tress, W.; Marinova, N.; Moehl, T.; Zakeeruddin, S. M.; Nazeeruddin, M. K.; Grätzel, M. Understanding the rate-dependent J–V hysteresis, slow time component, and aging in CH 3 NH 3 PbI 3 perovskite solar cells: the role of a compensated electric field. *Energ. Environ. Sci* **2015**, *8*, 995–1004.

(64) Lin, Q.; Armin, A.; Nagiri, R. C. R.; Burn, P. L.; Meredith, P. Electro-optics of perovskite solar cells. *Nat. Photonics* **2015**, *9*, 106–112.

(65) Ferdani, D.; Pering, S.; Ghosh, D.; Kubiak, P.; Walker, A.; Lewis, S. E.; Johnson, A. L.; Baker, P. J.; Islam, S.; Cameron, P. J. Partial Cation Substitution Reduces Iodide Ion Transport in Lead Iodide Perovskite Solar Cells. *Energ. Environ. Sci* **2019**,

(66) Henkelman, G.; Uberuaga, B. P.; Jonsson, H. Climbing image nudged elastic band

method for finding saddle points and minimum energy paths. *J. Chem. Phys* **2000**, *113*, 9901–9904.

(67) Eames, C.; Frost, J. M.; Barnes, P. R.; O'regan, B. C.; Walsh, A.; Islam, M. S. Ionic Transport in Hybrid Lead Iodide Perovskite Solar Cells. *Nat. Commun.* **2015**, *6*, 7497.

(68) Meloni, S.; Moehl, T.; Tress, W.; Franckevičius, M.; Saliba, M.; Lee, Y. H.; Gao, P.; Nazeeruddin, M. K.; Zakeeruddin, S. M.; Rothlisberger, U. Ionic polarization-induced current–voltage hysteresis in CH 3 NH 3 PbX 3 perovskite solar cells. *Nat. Commun.* **2016**, *7*, 10334.

(69) Kennard, R. M.; Dahlman, C. J.; Nakayama, H.; DeCrescent, R. A.; Schuller, J. A.; Seshadri, R.; Mukherjee, K.; Chabinyc, M. L. Phase stability and diffusion in lateral heterostructures of methyl ammonium lead halide perovskites. *ACS Appl. Energy Mater."* **2019**, *11*, 25313–25321.

(70) García-Rodríguez, R.; Ferdani, D.; Pering, S.; Baker, P. J.; Cameron, P. J. Influence of bromide content on iodide migration in inverted MAPb (I 1- x Br x) 3 perovskite solar cells. *J. Mater. Chem. A* **2019**, *7*, 22604–22614.

(71) Lin, C.; Li, S.; Zhang, W.; Shao, C.; Yang, Z. Effect of Bromine Substitution on the Ion Migration and Optical Absorption in MAPbI3 Perovskite Solar Cells: The First-Principles Study. *ACS Appl. Energy Mater."* **2018**, *1*, 1374–1380.

(72) Tisdale, J. T.; Muckley, E.; Ahmadi, M.; Smith, T.; Seal, C.; Lukosi, E.; Ivanov, I. N.; Hu, B. Dynamic Impact of Electrode Materials on Interface of Single-Crystalline Methylammonium Lead Bromide Perovskite. *Adv. Mater. Interfaces* **2018**, *5*, 1800476.

(73) Galkowski, K.; Mitioglu, A.; Miyata, A.; Plochocka, P.; Portugall, O.; Eperon, G. E.; Wang, J. T.-W.; Stergiopoulos, T.; Stranks, S. D.; Snaith, H. J. Determination of the exciton binding energy and effective masses for methylammonium and formamidinium lead tri-halide perovskite semiconductors. *Energ. Environ. Sci* **2016**, *9*, 962–970.

(74) Mosconi, E.; Umari, P.; De Angelis, F. Electronic and optical properties of MAPbX 3 perovskites (X= I, Br, Cl): a unified DFT and GW theoretical analysis. *Phys. Chem. Chem. Phys* **2016**, *18*, 27158–27164.

(75) Miyata, A.; Mitioglu, A.; Plochocka, P.; Portugall, O.; Wang, J. T.-W.; Stranks, S. D.; Snaith, H. J.; Nicholas, R. J. Direct measurement of the exciton binding energy and effective masses for charge carriers in organic–inorganic tri-halide perovskites. *Nature Physics* **2015**, *11*, 582.

(76) D'Innocenzo, V.; Grancini, G.; Alcocer, M. J.; Kandada, A. R. S.; Stranks, S. D.; Lee, M. M.; Lanzani, G.; Snaith, H. J.; Petrozza, A. Excitons versus free charges in organo-lead tri-halide perovskites. *Nat. Commun.* **2014**, *5*, 3586.

(77) Herz, L. M. Charge-carrier mobilities in metal halide perovskites: Fundamental mechanisms and limits. *ACS Energy Lett.* **2017**, *2*, 1539–1548.

(78) Yamada, T.; Aharen, T.; Kanemitsu, Y. Near-band-edge optical responses of CH 3 NH 3 PbCl 3 single crystals: photon recycling of excitonic luminescence. *Phys. Rev. Lett.* **2018**, *120*, 057404.

(79) Saba, M.; Quochi, F.; Mura, A.; Bongiovanni, G. Excited state properties of hybrid perovskites. *âĂŐAcc. Chem. Res* **2015**, *49*, 166–173.

(80) Manser, J. S.; Christians, J. A.; Kamat, P. V. Intriguing optoelectronic properties of metal halide perovskites. *Chem. Rev.* **2016**, *116*, 12956–13008.

(81) Sestu, N.; Cadelano, M.; Sarritzu, V.; Chen, F.; Marongiu, D.; Piras, R.; Mainas, M.; Quochi, F.; Saba, M.; Mura, A. Absorption F-sum rule for the exciton binding energy in methylammonium lead halide perovskites. *J. Phys. Chem. Lett* **2015**, *6*, 4566–4572.

(82) Tanaka, K.; Takahashi, T.; Ban, T.; Kondo, T.; Uchida, K.; Miura, N. Compara-

tive study on the excitons in lead-halide-based perovskite-type crystals CH3NH3PbBr3 CH3NH3PbI3. *Solid State Commun.* **2003**, *127*, 619–623.

(83) Yakunin, S.; Dirin, D. N.; Shynkarenko, Y.; Morad, V.; Cherniukh, I.; Nazarenko, O.; Kreil, D.; Nauser, T.; Kovalenko, M. V. Detection of gamma photons using solution-grown single crystals of hybrid lead halide perovskites. *Nat. Photonics* **2016**, *10*, 585.

(84) Nazarenko, O.; Yakunin, S.; Morad, V.; Cherniukh, I.; Kovalenko, M. V. Single crystals of caesium formamidinium lead halide perovskites: solution growth and gamma dosimetry. *NPG Asia Materials* **2017**, *9*, e373.

(85) Kresse, G.; Hafner, J. Ab initio molecular dynamics for liquid metals. *Phys. Rev. B* **1993**, *47*, 558.

(86) Kresse, G.; Hafner, J. Ab initio molecular-dynamics simulation of the liquid-metal–amorphous-semiconductor transition in germanium. *Phys. Rev. B* **1994**, *49*, 14251.

(87) Kresse, G.; Joubert, D. From ultrasoft pseudopotentials to the projector augmented-wave method. *Phys. Rev. B* **1999**, *59*, 1758.

(88) Perdew, J. P.; Burke, K.; Ernzerhof, M. Generalized Gradient Approximation Made Simple. *Phys. Rev. Lett.* **1996**, *77*, 3865.

(89) Grimme, S.; Antony, J.; Ehrlich, S.; Krieg, H. A consistent and accurate ab initio parametrization of density functional dispersion correction (DFT-D) for the 94 elements H-Pu. *J. Chem. Phys* **2010**, *132*, 154104.

(90) Leguy, A. M.; Goñi, A. R.; Frost, J. M.; Skelton, J.; Brivio, F.; Rodríguez-Martínez, X.; Weber, O. J.; Pallipurath, A.; Alonso, M. I.; Campoy-Quiles, M. Dynamic disorder, phonon lifetimes, and the assignment of modes to the vibrational spectra of methylammonium lead halide perovskites. *Phys. Chem. Chem. Phys* **2016**, *18*, 27051–27066.

(91) Ganose, A. M.; Jackson, A. J.; Scanlon, D. O. sumo: Command-line tools for plotting and analysis of periodic ab initio calculations. *J. Open Source Softw.* **2018**, *2*.

(92) Stoneham, A. M. *Theory of defects in solids: electronic structure of defects in insulators and semiconductors*; Oxford University Press: Oxford, UK, 2001.